ADVANCED PHYSICS RESEARCH Open Access
www.advphysicsres.com

Double-Site Occupation Triggered Broadband and Tunable NIR-I and NIR-II Luminescence in $AlNbO_4:Cr^{3+}$ Phosphors

*Kuangnan Lyu, Gaochao Liu, Maxim S. Molokeev, and Zhiguo Xia**

Near-infrared (NIR) phosphor-converted light-emitting diodes (pc-LEDs) are desired for optoelectronic and biomedical applications, while the development of target broadband NIR phosphors still remains a significant challenge. Herein, a kind of Cr^{3+}-doped $AlNbO_4$ phosphors with a broad NIR emission ranging from 650 to 1400 nm under 450 nm excitation are reported. A giant red-shift emission peak from 866 to 1020 nm together with broadened full width at half-maximum of 320 nm is achieved simply by varying the doped Cr^{3+} concentrations. Structural and spectroscopy analysis demonstrate that a concentration-dependent site-occupation of Cr^{3+} emitters in different Al^{3+} sites is responsible for the tunable NIR luminescence. The as-fabricated NIR pc-LED based on optimized $AlNbO_4:Cr^{3+}$ phosphor exhibits great potential in night-vision applications. This work provides a novel design principle on the Cr^{3+}-doped $AlNbO_4$ phosphor with tunable broadband luminescence from NIR-I to NIR-II, and these materials can be employed in NIR spectroscopy applications.

1. Introduction

Broadband near-infrared (NIR) light source plays an unprecedented role in the fields of food quality inspection and analysis, night vision, medical diagnosis, and non-destructive monitoring, which accordingly has been widely studied as a hotspot in recent years.[1–6] In particular, the C—H, O—H, and N—H groups in different organics have characteristic absorption signals in 700–1100 nm, hence the NIR light source devices with broad emission bands are of great interest for component analysis.[2,7,8] However, it is apparent that the traditional NIR light sources, such as tungsten halogen lamps, NIR light-emitting diode (LED) arrays, and super-continuum lasers, suffer from the disadvantages of large size, poor efficiency, high spherical temperature, long response time, and high cost.[9–11] On the contrary, NIR phosphor-converted light-emitting diodes (pc-LEDs) based on the efficient blue InGaN chips are recognized as ideal candidates due to their low cost, tunable spectrum, good durability, and so on, which also perfectly meet the rapid development trend of wearable, multi-functional portable intelligent electronic products.[12,13] Therefore, developing efficient and thermally stable NIR phosphors that can be pumped by blue chips and emit in a wide spectral range has become a hot issue.

To fulfill the demands for the emerging photonic applications, intensive efforts have been made to exploit broadband NIR phosphors via rare earth ion- (Eu^{2+}), transition metal ion- (Cr^{3+}, Ni^{2+}, Mn^{4+}), or Bi ion-activated inorganic matrices.[14–17] However, the luminescence of Eu^{2+} and Mn^{4+} doped phosphors is hard to achieve NIR emission exceeding 800 nm, which limits some applications.[18] Moreover, Ni^{2+} and Bi ion-doped powders or glass materials usually exhibit ultra-broadband emission in the second near-infrared window (NIR-II), which suffers from low luminous efficiency.[19,20] On the contrary, the Cr^{3+} ion has

K. Lyu, G. Liu, Z. Xia
The State Key Laboratory of Luminescent Materials and Devices
Guangdong Provincial Key Laboratory of Fiber Laser Materials and Applied Techniques
Guangdong Engineering Technology Research and Development Center of Special Optical Fiber Materials and Devices
School of Materials Science and Engineering
South China University of Technology
Guangzhou 510641, P. R. China
E-mail: xiazg@scut.edu.cn

The ORCID identification number(s) for the author(s) of this article can be found under https://doi.org/10.1002/apxr.202200056

DOI: 10.1002/apxr.202200056

M. S. Molokeev
Laboratory of Crystal Physics
Kirensky Institute of Physics
Federal Research Center KSC SB RAS
Krasnoyarsk 660036, Russia

M. S. Molokeev
Department of Engineering Physics and Radioelectronic
Siberian Federal University
Krasnoyarsk 660041, Russia

M. S. Molokeev
Research and Development Department
Kemerovo State University
Kemerovo 650000, Russia

Z. Xia
School of Physics and Optoelectronics
South China University of Technology
Guangzhou 510641, P. R. China

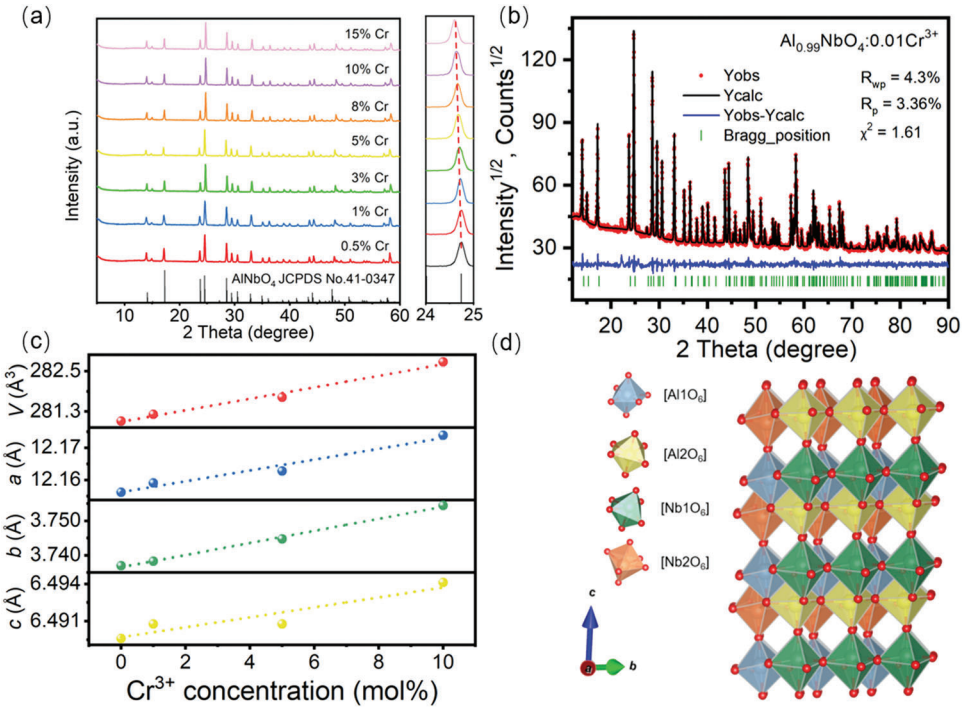

Figure 1. a) XRD patterns of $Al_{1-x}NbO_4$: xCr^{3+} (x = 0–0.15) and the standard data of $AlNbO_4$ phase with JCPDS No. 41–0347. b) Rietveld refinement of the typical XRD pattern of $Al_{0.99}NbO_4$: $0.01Cr^{3+}$. c) The cell parameters and volume change of $Al_{1-x}NbO_4$: xCr^{3+} (x = 0–0.15) depending on Cr^{3+} concentration. d) Schematic crystal structure diagram of $AlNbO_4$ host and different coordination spheres.

been considered as an ideal NIR emission center, which exhibits excellent tunable emission covering from 650 to 1600 nm and a broad absorption band that matches well with commercial blue chips.[21] For instance, Cr^{3+}-activated $Ca_2LuZr_2Al_3O_{12}$ phosphors exhibit 69.1% NIR luminous efficiency with excellent thermal stability (70%@150 °C) under the 460 nm excitation.[22] $Sr_9M(PO_4)_7$:Cr^{3+} (M = Ga, Sc, In, and Lu) phosphors were reported with suppressed concentration quenching effect, and the optimal $Sr_9Ga_{0.2}(PO_4)_7$:$0.8Cr^{3+}$ demonstrates a high external quantum efficiency (EQE) above 30%.[23] However, the emission spectra of most Cr^{3+}-doped NIR phosphors are located in the NIR-I region (700–900 nm), which is insufficient to meet the demands of long-wavelength NIR light for food analysis applications. Although $Cs_2AgInCl_6$:Cr^{3+} was recently reported and displayed a long-wavelength NIR luminescence centered at 1010 nm, it cannot be activated by blue chips.[24] Therefore, the development of tunable long-wavelength ultra-broadband NIR phosphors that can be excited by blue chips remains a great challenge. Designing different luminescence centers in a single host is recognized as a general strategy to broaden its emission spectrum. In this respect, co-doping Yb^{3+} ions has become an effective method to broaden the emission band of Cr^{3+} over 1000 nm with enhanced quantum efficiency and thermal stability, which is attributed to the efficient energy transfer process from Cr^{3+} to Yb^{3+}.[2,25] Furthermore, introducing Cr^{4+} ions on Cr^{3+}-doped phosphors seems to be another way to extend its emission spectrum to NIR-II region, such as $Mg_{14}Ge_5O_{24}$:Cr^{3+} and Cr^{4+}, which may lead to an obvious absorption in the NIR spectral range.[26] Besides, multiple-site occupation by Cr^{3+} is regarded as a promising method to reach ultra-broadband emission. For example, Li_2MgZrO_6:Cr^{3+} phosphor exhibits a broadband emission with a large FWHM of 210 nm, benefiting from the two Cr^{3+} ions in different Mg and Zr sites.[27] The ultra-broadband NIR emission of $GaGe_4O_8$:Cr^{3+} is realized by three different Cr^{3+}-emitting centers with various crystal field strengths.[28] In general, the development of long-wavelength ultra-broadband NIR phosphors is still a challenge, and the multiple-sites occupancy engineering of Cr^{3+} in NIR phosphors is supposed to be a promising strategy.

In this work, we report the discovery of Cr^{3+}-doped $AlNbO_4$ phosphors and the photoluminescence (PL) tuning. Under 450 nm irradiation, $Al_{0.99}NbO_4$:$0.01Cr^{3+}$ depicts a broadband emission ranging from 650 to 1400 nm with a full width at half-maximum (FWHM) of 244 nm. With increasing of Cr^{3+} ion concentration, the luminescent spectra show dramatically red-shift from 866 to 1020 nm, with broadened FWHM to 322 nm. The origin of the tunable and ultra-broadband emission band is ascribed to the double-site occupancy by Cr^{3+} at Al^{3+} sites, which is also confirmed by the structural and low-temperature spectroscopy analysis. Finally, the NIR pc-LED is fabricated by $Al_{0.99}NbO_4$:$0.01Cr^{3+}$ phosphor, and it displays excellent application potential in night-vision and component analysis.

2. Results and Discussion

2.1. Phase and Crystal Structure

X-ray diffraction (XRD) patterns of as-prepared $Al_{1-x}NbO_4$: xCr^{3+} (x = 0 – 0.15) samples are illustrated in **Figure 1**a. All the diffraction peaks are well indexed to the standard data of the $AlNbO_4$ phase (JCPDS 41–0347), demonstrating the successful

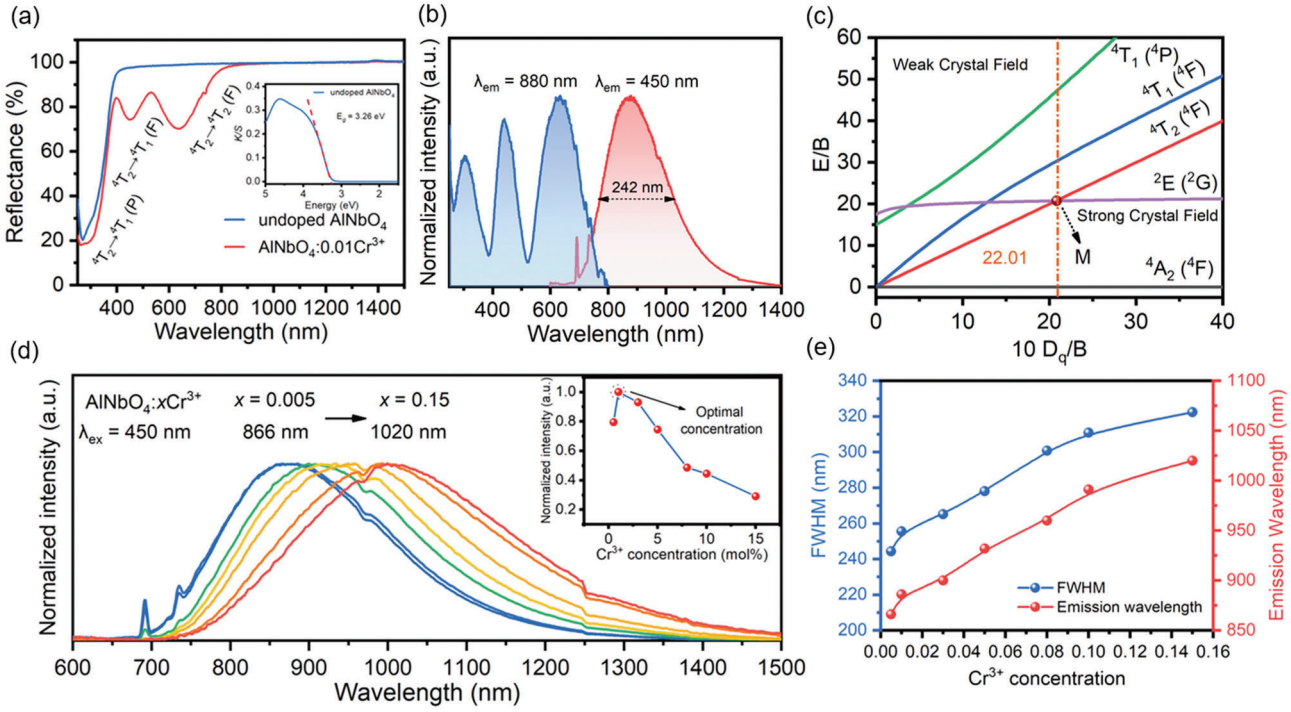

Figure 2. a) Diffuse reflectance spectra of $Al_{1-x}NbO_4$:xCr^{3+} ($x = 0$ and 0.01). b) Room temperature PLE and PL spectra of $Al_{0.99}NbO_4$:$0.01Cr^{3+}$ phosphor. c) Tanabe–Sugano energy level diagram for Cr^{3+} ions ($3d^3$) in octahedral coordination. The point of M ($10\,D_q/B = 23$) means the intersection of ^2E and $^4T_2$ (^4F) energy levels and the division of weak and strong crystal fields. d) Normalized PL spectra of $Al_{1-x}NbO_4$:xCr^{3+} ($x = 0$–0.15). The inset represents plots of integrated intensities versus Cr^{3+} concentrations. e) FWHM and emission wavelength of $Al_{1-x}NbO_4$:xCr^{3+} ($x = 0$–0.15) as a function of Cr^{3+} concentration.

phase formation of the desired samples. The characteristic XRD peaks shift slightly toward a low angle in the enlarged 2θ range of 24°– 25° with increasing Cr^{3+} concentration, also indicating that the Cr^{3+} ions have been successfully incorporated into the host lattice. To further demonstrate the crystal structure, Rietveld refinement was performed by TOPAS 4.2 software, and the results of $Al_{1-x}NbO_4$: xCr^{3+} ($x = 0 - 0.15$) are shown in Figure 1b and Figure S1, Supporting Information, respectively. All the experimental peaks match well with the calculated results. The detailed refinement statistics are listed in Table S1, Supporting Information. Moreover, the changes in cell parameters (*a*, *b*, *c*) and volume (*V*) with increasing Cr^{3+} concentration are shown in Figure 1c. The detailed atomic coordinates and isotropic displacement parameters are listed in Table S2, Supporting Information. It is notable that the values of cell parameters and volume increase with increasing Cr^{3+} concentration, which is in agreement with the XRD peaks shifting toward lower angles. Figure 1d depicts the crystal structure of $AlNbO_4$, which crystallizes in a monoclinic crystal structure with the space group of *C*2/*m*. In the $AlNbO_4$ structure, Al^{3+} and Nb^{5+} ions are both coordinated by six O^{2-} ions forming [AlO_6] and [NbO_6] octahedra with edge-sharing connections. Al^{3+} and Nb^{5+} ions are placed in two octahedra, named Al1/Al2 and Nb1/Nb2, respectively. It is notable that different [AlO_6] and [NbO_6] octahedra have slightly different average Al—O and Nb—O bond lengths, listed in Table S3, Supporting Information. By considering valance and ionic radii of Al^{3+} ($r = 0.54$ Å, when CN = 6), Nb^{5+} ($r = 0.64$ Å, when CN = 6), and Cr^{3+} ($r = 0.62$ Å, when CN = 6), the substitution of Cr^{3+} ions into the crystal structure is expected to occur on the Al^{3+} ions.

2.2. Photoluminescence Properties

Figure 2a depicts the diffuse reflectance spectra of $Al_{1-x}NbO_4$:xCr^{3+} ($x = 0$ and 0.01). The bandgap of the $AlNbO_4$ matrix is estimated to be ≈3.26 eV via the extrapolated line in the Kubelka–Munk absorption spectrum.[29] After Cr^{3+} doping, three extra absorption bands peaking at 285, 450, and 640 nm can be observed, which are attributed to $^4A_2 \rightarrow {}^4T_1$ (^4P), $^4A_2 \rightarrow {}^4T_1$ (^4F), and $^4A_2 \rightarrow {}^4T_2$ (^4F) transitions of Cr^{3+} ions, respectively. Moreover, no obvious characteristic absorption bands of Cr^{4+} ions (600–1160 nm), can be found in Figure 2a, indicating that no transition of Cr^{4+} ions occurs in this system.[30] Room temperature PL and PL excitation (PLE) spectra of $Al_{0.99}NbO_4$:$0.01Cr^{3+}$ are given in Figure 2b. Under 450 nm excitation, the phosphor exhibits a broadband emission peaking at 880 nm and ranges from 650 to 1400 nm with a large FWHM of 242 nm, which originates from the spin-allowed transition of Cr^{3+} ions in octahedral coordination. Besides, the weak line emission around 700 nm is also detected for $Al_{0.99}NbO_4$:$0.01Cr^{3+}$, which is ascribed to the spin-forbidden $^2E \rightarrow {}^4A_2$ transition of Cr^{3+} ions in the octahedral coordination site. Moreover, a continuous broad PLE spectrum ranging from 250 to 800 nm can be acquired, and three bands located at 285, 450, and 640 nm are observed when monitoring

at the maximum emission, which should be assigned to the $^4A_2 \rightarrow {}^4T_1$ (^4P), $^4A_2 \rightarrow {}^4T_1$ (^4F), and $^4A_2 \rightarrow {}^4T_2$ (^4F) transitions of Cr^{3+} ions, respectively.[31] The excitation band around 450 nm matches well with the emission spectrum of the blue LED chip, which further indicates that $Al_{0.99}NbO_4$:$0.01Cr^{3+}$ can be applied in commercial devices.

It is well known that the valence electrons of Cr^{3+} ions are not shielded by the shell and interact strongly with the crystal field and lattice vibrations due to the spatial extension of the *d* electron wavefunction in the crystals, thus making the optical properties of Cr^{3+}-doped phosphors tunable.[32] When considering Cr^{3+} ions in the center of coordinated octahedrons, the crystal field strength is determined by Equations (1)–(3)

$$10D_q = E\left({}^4T_2\right) = E\left({}^4A_2 \rightarrow {}^4T_2\right) \tag{1}$$

$$B = D_q \frac{x^2 - 10x}{15\,(x-8)} \tag{2}$$

$$x = \frac{E\left({}^4T_1\right) - E({}^4T_2)}{D_q} = \frac{E({}^4A_2 \rightarrow {}^4T_1) - E({}^4A_2 \rightarrow {}^4T_2)}{D_q} \tag{3}$$

where D_q denotes the crystal field strength, $E(^4T_2)$ and $E(^4T_1)$ are the equilibrium positions of the $^4T_2$ (^4F) and $^4T_1$ (^4F) energy levels for Cr^{3+} ions, and $E(^4A_2 \rightarrow {}^4T_2)$ and $E(^4A_2 \rightarrow {}^4T_1)$ represent the corresponding transition energies.[33] Tanabe–Sugano energy level diagram of Cr^{3+} in an octahedral coordination environment is shown in Figure 2c. The crystal field parameter D_q/B is finally determined to be 2.32 for $Al_{0.99}NbO_4$:$0.01Cr^{3+}$, which is slightly bigger than Cr^{3+} in a weak crystal field ($D_q/B < 2.3$). This suggests that the matrix provides a relatively weak crystal field for a doped Cr^{3+} emitter.

According to the Tanabe–Sugano energy level diagram of Cr^{3+}, the emission spectrum of Cr^{3+} ions in the center of coordinated octahedrons is related to the surrounding crystal field. In general, the emission spectrum of Cr^{3+} can be dramatically changed by ion substitution due to the local structure regulation. However, varying the Cr^{3+} concentration is a more convenient strategy to realize a tunable emission spectrum of $AlNbO_4$:Cr^{3+}. The normalized emission spectra of $Al_{1-x}NbO_4$:xCr^{3+} (x = 0.005–0.15) are shown in Figure 2d. Under 450 nm excitation, a large redshift of the emission peaks from 866 to 1020 nm can be acquired for $Al_{1-x}NbO_4$:xCr^{3+} phosphors with increasing x values from 0.005 to 0.15. The inset of Figure 2d and Figure S2, Supporting Information, depict that the PL intensity reaches its maximum when x is 0.01, and then, the concentration quenching effect occurs with increasing x values. Furthermore, the relation among Cr^{3+} concentration, emission wavelength, and FWHM is shown in Figure 2e. All the samples demonstrate the ultra-broad band emission ranging from 700 to 1400 nm, and the FWHM increases from 244 to 322 nm with increasing x values. The crystal field strength of $Al_{1-x}NbO_4$:xCr^{3+} with different Cr^{3+} contents is listed in Table S4, Supporting Information. The concentration-dependent redshift can be explained by the combined effect of crystal field, reabsorption, and energy transfer variations.[34,35] Two Al^{3+} sites in $AlNbO_4$ for Cr^{3+} substitution can provide different Cr^{3+}-emitting centers in $AlNbO_4$:Cr^{3+}, which is responsible for this dramatic spectral shift and will be further discussed later. Moreover, the quantum efficiencies were measured to estimate the luminescence properties of $Al_{0.99}NbO_4$:$0.01Cr^{3+}$. The internal quantum efficiency (IQE) and EQE are 37.4% and 21.8%, respectively, as shown in Figure S3, Supporting Information. The relatively low IQE may be attributed to the violent non-radiation relaxation process, which should be improved by further composition modifications.

2.3. Multiple-Site Cr^{3+} Emission Mechanism

As shown in Figure S4, Supporting Information, the room temperature PL decay curve of $Al_{0.99}NbO_4$:$0.01Cr^{3+}$ was measured by pumping the phosphor at 450 nm and monitoring at 880 nm. The decay curve can be well fitted by a bi-exponential formula as follows

$$I\ (t) = A_1\ \exp\left(-t/\tau_1\right) + A_2 \exp\left(-t/\tau_2\right) \tag{4}$$

where $I(t)$ is the emission intensity at a certain time t, A_1 and A_2 are constants, and τ_1 and τ_2 are the decay times. The fitting results for $Al_{0.99}NbO_4$:$0.01Cr^{3+}$ are 6.13 and 1.52 μs, and the average lifetime was approximately calculated to be 4.36 μs based on the following relationships

$$\tau_{ave} = \frac{A_1\tau_1^2 + A_2\tau_2^2}{A_1\tau_1 + A_2\tau_2} \tag{5}$$

Figure 3a depicts the PL decay curves of $Al_{1-x}NbO_4$:xCr^{3+} with various x values upon excitation at 450 nm. The photoluminescence shows a faster decay with increasing Cr^{3+} content due to the increased non-radiative transitions. All the decay curves are well-fitted with a bi-exponential function. These results support that there are two different Cr^{3+}-emitting centers in this system, named Cr1 and Cr2, respectively. It is well known that emitting center in a strong crystal field usually has a longer decay time.[36] Based on the structural analysis results mentioned above, Cr1 ions are supposed to occupy octahedrally coordinated Al1 sites with the shorter average bond length, which are located at a relatively stronger crystal field. Similarly, Cr2 ions are supposed to occupy octahedrally coordinated Al2 sites with longer average bond lengths.

To investigate the detailed luminescence mechanism of $AlNbO_4$:Cr^{3+}, temperature-dependent PL spectra of $Al_{0.99}NbO_4$:$0.01Cr^{3+}$ was checked and given in Figure S5a, Supporting Information. Compared with the PL spectrum at room temperature, an obvious new emission peaking at 756 nm is observed in the PL spectrum at 77 K, which suggests the existence of two kinds of octahedral sites occupied by Cr^{3+} ions. As the temperature increases, the PL intensity of emission monitored at 756 nm gradually declined until disappeared at room temperature, which may be attributed to the thermal quenching effect.[37] The normalized PL intensity of $Al_{0.99}NbO_4$:$0.01Cr^{3+}$ upon 450 nm excitation between 77 and 400 K is shown in Figure S5b, Supporting Information. The PL spectra of $Al_{0.99}NbO_4$:$0.01Cr^{3+}$ and $Al_{0.95}NbO_4$:$0.05Cr^{3+}$ upon excitation at 450 nm under 77 K are shown in Figures 3b and 3c, respectively. All the PL spectra are well decomposed into two Gaussian curves, which depict that Cr^{3+} ions occupy two different sites. Apparently, the contribution of Cr1 ions decreases with

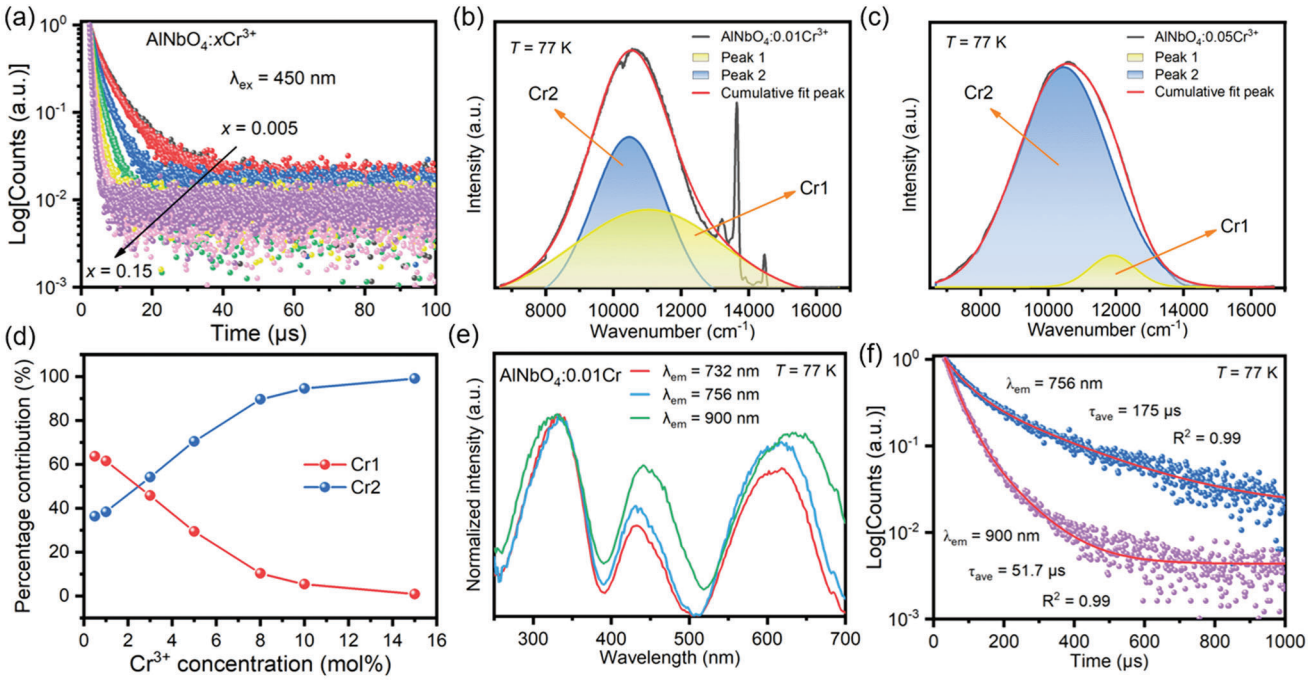

Figure 3. a) Room temperature PL decay curves of $Al_{1-x}NbO_4$:xCr^{3+} (x = 0–0.15) upon excitation at 450 nm. The Gaussian fitting curves of b) $Al_{0.99}NbO_4$:$0.01Cr^{3+}$ and c) $Al_{0.95}NbO_4$:$0.05Cr^{3+}$ upon excitation at 450 nm recorded at 77 K. d) Percentage contribution values of Cr^{3+} emitter centers in $AlNbO_4$:Cr^{3+} with various Cr^{3+} concentrations. e) Normalized PLE spectra monitored at 732, 756, and 900 nm, respectively, upon 450 nm excitation under 77 K. f) PL decay curves of $Al_{0.99}NbO_4$:$0.01Cr^{3+}$ monitored at 756 and 900 nm under 77K, respectively.

higher Cr^{3+} concentration, while the contribution of Cr2 ions increases as a comparison. This result confirms that the giant redshift of PL spectra is ascribed to the varying contribution of Cr1 and Cr2 ions with different Cr^{3+} concentrations. Theoretically, the Cr2 centers with longer emission wavelengths are characteristic of more severe non-radiative relaxation and poor thermal resistance. Hence, a blue-shift of emission peak with rising temperature is expected to be observed as shown in Figure S5, Supporting Information, further verifying the double-sites occupation of Cr^{3+} in the $AlNbO_4$ host.[38]

As discussed above, broadband emission mainly originates from two Cr^{3+} centers. Herein, the calculated percentage contribution values and fitted lifetimes of Cr1 and Cr2 centers in $Al_{1-x}NbO_4$:xCr^{3+} are given in Figure 3d and Figure S6, Supporting Information, respectively. The photoluminescent contribution from Cr2 increases for $Al_{1-x}NbO_4$:xCr^{3+} upon doping more Cr^{3+} ions, and the contribution from Cr1 decreases accordingly. Moreover, the lifetime values of Cr1 and Cr2 are simultaneously shortened with increasing Cr^{3+} content. In general, the ultra-broadband emission is attributed to two different Cr^{3+} centers in $Al_{1-x}NbO_4$:xCr^{3+}. Furthermore, the occupancy of the site can be effectively investigated by checking PLE spectra monitored at corresponding emissions. The normalized PLE spectra monitored at 732, 756, and 900 nm are presented in Figure 3e. As monitored at 732 and 756 nm, no obvious difference was observed, which suggests that two sharp emissions originate from the same Cr^{3+} octahedral site with a relatively stronger crystal field strength. In addition, as monitored at 900 nm, which relates to the broadband emission peak, a visible difference was observed in the band absorption positions, compared with two sharp emissions monitored at 732 and 756 nm. Furthermore, PL decay curves of $Al_{0.99}NbO_4$:$0.01Cr^{3+}$ at 77 K were detected and are shown in Figure 3f, which was excited at 450 nm and monitored at 756 and 900 nm. All decay curves can be well fitted by a bi-exponential Equation (4), and the average decay times are calculated by Equation (5). The lifetimes of the emission peaks located at 756 and 900 nm are calculated as 175 and 51.7 μs, respectively. It is apparent that the lifetime of a sharp peak (756 nm) is much longer than that of broadband (900 nm). Considering the influence of spin-forbidden transitions, the shorter exponential component τ_2 related to the intrinsic broadband emission was fitted to be 55.2 and 33.6 μs, respectively, which suggests that they originate from two different Cr^{3+} sites.

2.4. Application of NIR pc-LED

Finally, the potential application of optimized $AlNbO_4$:Cr^{3+} phosphors was demonstrated in this work. As shown in **Figure 4**a, a NIR pc-LED lamp was fabricated by combining the as-prepared $Al_{0.99}NbO_4$:$0.01Cr^{3+}$ phosphor with a commercial 460 nm blue InGaN chip. Figure 4b depicts the schematic diagram of the NIR pc-LED imaging device showing the application principle. Under the driven current, the light of the fabricated NIR pc-LED can be exposed to the detected objects, and the images of objects can be captured through the NIR camera. To demonstrate the potential application of $Al_{0.99}NbO_4$:$0.01Cr^{3+}$ phosphor in NIR pc-LED, the images of flowers under natural light and NIR pc-LED are shown

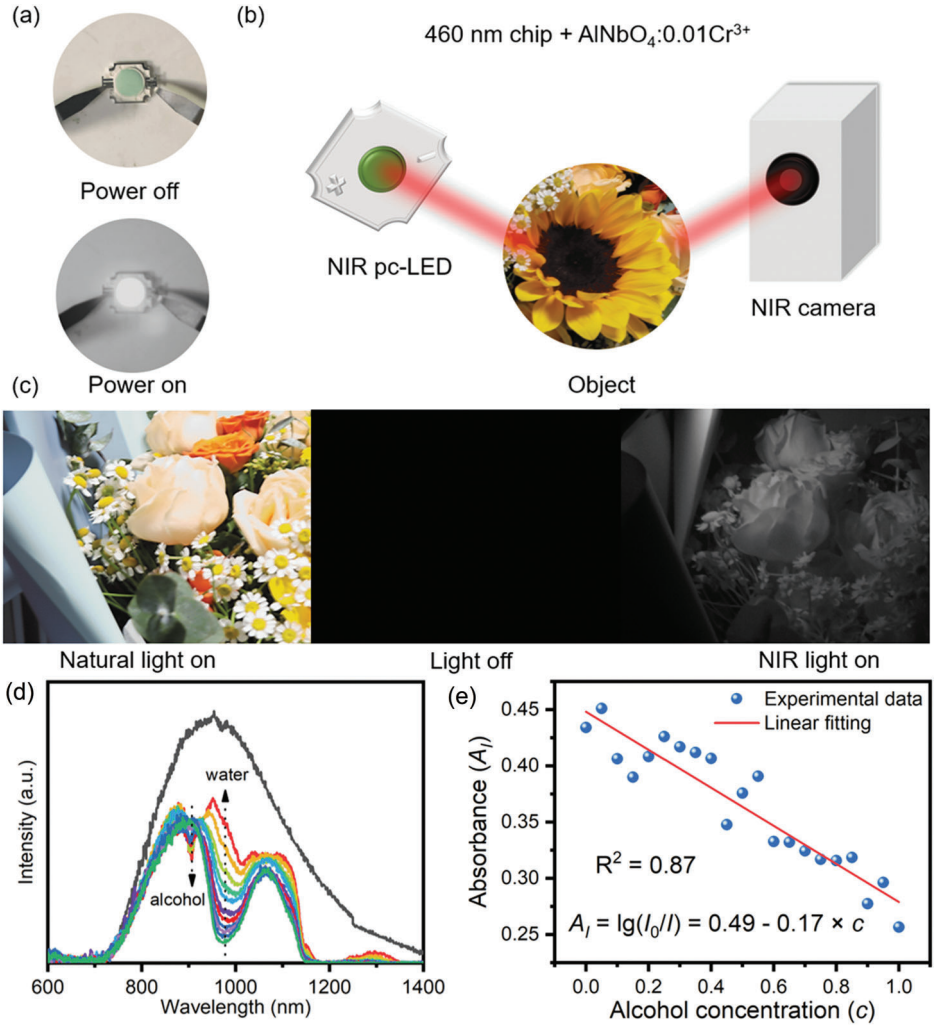

Figure 4. a) Picture of the as-fabricated NIR pc-LED with power off and on (with a 720 nm filter). b) Schematic diagram of NIR pc-LED imaging device showing the application principle. c) Visible and NIR images of the flowers. d) NIR transmittance spectra of mixed solutions of water and alcohol in different proportions by using $Al_{0.9}NbO_4$:$0.1Cr^{3+}$ phosphor. e) Functional relationship between alcohol concentration and NIR light absorbance based on the as-fabricated NIR device.

in Figure 4c. The flower can be clearly captured under the irradiation of the fabricated NIR pc-LED. These images indicated that the phosphor has the potential to be a new candidate for night-vision application.

As mentioned previously, different kinds of functional groups, such as C—H, N—H, and O—H, with various energy levels can absorb NIR light in accordance with their unique vibrational frequency. NIR spectroscopy is regarded as a highly efficient method for qualitative and quantitative analysis in the food and agricultural industries. To demonstrate the potential application in the field of NIR spectroscopy technology, the transmission spectra of mixed solutions of water and alcohol were detected, which were pumped by NIR-emitting $Al_{0.9}NbO_4$:$0.1Cr^{3+}$ phosphor. Figures S7a and S7b, Supporting Information, depict the PL spectra of $Al_{0.9}NbO_4$:$0.1Cr^{3+}$ after penetrating water and absolute ethanol, respectively. The transmission spectra show characteristic NIR absorption bands of water at 960 and 1160 nm, while ethanol at 905, 1010, and 1185 nm. The transmittance spectra were detected after passing through various mixed solutions of water and alcohol with a proportion of absolute alcohol from 0% to 100% with an interval of 5%, shown in Figure 4d. Compared with the original PL spectrum, two obvious absorption bands peaking at 910 and 970 nm were displayed in all transmittance spectra, which can be ascribed to the characteristic absorption of absolute alcohol and water, respectively. With the increase in the proportion of absolute alcohol, the intensity of peaking at 910 nm decreased, however, the intensity of peaking at 970 nm raised. The relationship was established based on the Lambert–Beer law, as given below

$$A_l = \lg\left(\frac{I_0}{I}\right) = \varepsilon l c \tag{6}$$

where A_l represents the absorbance of a certain component in a transparent solution and ϵ means its molar absorptivity, l is the optical path length during the test, and c represents the

concentration of the light-absorbing component in the solution. I_0 and I are the initial and transmissive intensities of the light. The dependence between alcohol concentration and absorbance as shown in Figure 4e, which can be calculated and fitted by a linear relationship with an R^2 value of 87%. Therefore, by detecting the transmittance spectrum, the alcohol concentration in a mixed solution of absolute alcohol and water with random proportions can be calculated using the fitted function mentioned above. Finally, one can find that the transmittance spectrum by $AlNbO_4$:Cr^{3+} phosphor-based NIR light source has a promising potential to be used in the field of quantitative component identification.

3. Conclusion

In summary, we have designed the novel broad-band NIR-emitting $Al_{1-x}NbO_4$:xCr^{3+} ($x = 0 - 0.15$) phosphors with tunable photoluminescence behaviors. Under 450 nm excitation, $Al_{1-x}NbO_4$:xCr^{3+} phosphors exhibit broadband NIR emissions ranging from 650 to 1400 nm with the FWHM up to 244 nm. With increasing Cr^{3+} concentration, the NIR emission peaks show a dramatic redshift from 866 to 1020 nm. Besides, the FWHM of the samples is broadened up to 322 nm depending on the increasing Cr^{3+} concentration. Structural and low-temperature spectra analysis confirm that double Al^{3+} sites with different coordination environments exist in $Al_{1-x}NbO_4$:xCr^{3+}, and therefore, the two different Cr^{3+} emission centers and the energy transfer between them benefit the tunable ultra-broadband NIR emissions. Finally, a NIR pc-LED device is fabricated by optimized $AlNbO_4$:Cr^{3+} phosphor, and a night-visible image and transmittance spectra are captured, suggesting that the phosphor has great potential for NIR spectroscopy applications.

4. Experimental Section

Synthesis: $Al_{1-x}NbO_4$: xCr^{3+} (x = 0–0.15) phosphors were synthesized by a facile solid-state reaction method. Highly pure Al_2O_3 (99.99%, Aladdin), Nb_2O_5 (99.99%, Aladdin), and Cr_2O_3 (99.99%, Aladdin) powders as raw materials were weighed according to the stoichiometric ratios, then grounded in an agate mortar for about 15 min for complete mixing. The mixtures were decanted into an aluminum oxide crucible and sintered at 1500 °C for 6 h in air. Afterward, the final products were ground into a fine powder using an agate mortar and pestle.

Fabrication of NIR pc-LEDs: The NIR pc-LEDs were fabricated by coating the optimal phosphor $Al_{0.99}NbO_4$: $0.01Cr^{3+}$ onto blue InGaN LED chips. The mass ratio of phosphor to epoxy resin was fixed at 1:1. The blue InGaN chips in the COB LEDs are (S-35EBMUD-A, 450–452.5 nm, 2.9–3.1V/150 mA, San'an Optoelectronics co., LTD., China).

Characterization: The phase and purity of the as-prepared powder samples were examined by XRD using a Bruker D8 ADVANCE power diffractometer with CuKα radiation source (λ = 0.15406 nm) and a linear VANTEC detector. The operation voltage and current were set as 40 kV and 15 mA, respectively. The data were collected in the range of 5°–90° with a step size of 0.0217° (2θ) and a count time of 5 s per step. Structural characterization and Rietveld refinement were conducted using TOPAS 4.2 software. Room-temperature PL spectra and PLE spectra were recorded using an FLS1000 fluorescence spectrophotometer equipped with a continuous xenon lamp (450 W) as an excitation source and a liquid-nitrogen-cooled NIR photomultiplier tube as a detector (Hamamatsu, R5509, InP/InGaAsP). The PL decay curve was also measured by the same FLS1000 instrument using a microsecond flash lamp (μF900) as the excitation source, and the statistical photons are 5000. The luminescence thermal quenching behavior of the samples was measured by the same spectrophotometer, which was equipped with a TAP-02 high-temperature fluorescence instrument (Tian Jin Orient-KOJI Instrument Co., Ltd.). The temperature-dependent spectra were measured by the same spectrophotometer equipped with the cryogenic liquid helium plant equipment. Photographs for the application of NIR pc-LEDs were taken by an industrial night-vision camera (MV-CA050-20GN, HIKVISION, China). The diffuse reflection (DR) spectra of the samples were recorded using a UV–vis-NIR spectrophotometer (Hitachi High-Tech Science Corporation, UH4150) with $BaSO_4$ as a standard. The quantum efficiency at room temperature was measured by an absolute PL quantum yield spectrometer (Quantaurus – QY Plus C13534-12, Hamamatsu Photonics). The demonstration images were collected by an industrial night-vision camera (MV-CA050-20GN, HIKVISION, China).

Supporting Information

Supporting Information is available from the Wiley Online Library or from the author.

Acknowledgements

This research was supported by the International Cooperation Project of the National Key Research and Development Program of China (2021YFB3500400 and 2021YFE0105700), National Natural Science Foundations of China (Grant No. 51972118), Guangzhou Science & Technology Project (202007020005), the State Key Laboratory of Luminescent Materials and Devices (Skllmd-2022-02), and the Local Innovative and Research Teams Project of Guangdong Pearl River Talents Program (2017BT01×137). This work was also funded by RFBR according to the research project No. 19-52-80003.

Conflict of Interest

The authors declare no conflict of interest.

Data Availability Statement

The data that support the findings of this study are available from the corresponding author upon reasonable request.

Keywords

near-infrared luminescence, phosphor, site occupation, tunable emissions

Received: October 4, 2022
Revised: November 4, 2022
Published online: December 15, 2022

[1] B. Grassi, V. Quaresima, *J. Biomed. Opt.* **2016**, *21*, 091313.
[2] G. Liu, T. Hu, M. S. Molokeev, Z. Xia, *iScience* **2021**, *24*, 102250.
[3] L. S. Magwaza, U. L. Opara, H. Nieuwoudt, P. J. R. Cronje, W. Saeys, B. Nicolaï, *Food Bioprocess Technol.* **2011**, *5*, 425.
[4] M. Manley, *Chem. Soc. Rev.* **2014**, *43*, 8200.
[5] F. Scholkmann, S. Kleiser, A. J. Metz, R. Zimmermann, J. M. Pavia, U. Wolf, M. Wolf, *NeuroImage* **2014**, *85*, 6.
[6] F. Zhao, Z. Song, Q. Liu, *Laser Photonics Rev.* **2022**, *16*, 2200380.
[7] J. Qiao, G. Zhou, Y. Zhou, Q. Zhang, Z. Xia, *Nat. Commun.* **2019**, *10*, 5267.
[8] M. Yu, Y. Okawachi, R. Cheng, C. Wang, M. Zhang, A. L. Gaeta, M. Loncar, *Light: Sci. Appl.* **2020**, *9*, 9.

[9] V. V. Alexander, O. P. Kulkarni, M. Kumar, C. Xia, M. N. Islam, F. L. Terry, M. J. Welsh, K. Ke, M. J. Freeman, M. Neelakandan, A. Chan, *Opt. Fiber Technol.* **2012**, *18*, 349.
[10] A. Christensen, S. Graham, *Appl. Therm. Eng.* **2009**, *29*, 364.
[11] V. Rajendran, M. Fang, G. N. D. Guzman, T. Lesniewski, S. Mahlik, M. Grinberg, G. Leniec, S. M. Kaczmarek, Y. Lin, K. Lu, C. Lin, H. Chang, S. Hu, R. Liu, *ACS Energy Lett.* **2018**, *3*, 2679.
[12] Z. Yang, Y. Zhou, J. Qiao, M. S. Molokeev, Z. Xia, *Adv. Opt. Mater.* **2021**, *9*, 2100131.
[13] J. Zhong, Y. Zhuo, F. Du, H. Zhang, W. Zhao, J. Brgoch, *ACS Appl. Mater. Interfaces* **2021**, *13*, 31835.
[14] J. Du, O. Q. De Clercq, K. Korthout, D. Poelman, *Materials* **2017**, *10*, 1422.
[15] G. Feng, S. Zhou, J. Bao, X. Wang, S. Xu, J. Qiu, *J. Alloys Compd.* **2008**, *457*, 506.
[16] Z. Gao, Y. Liu, J. Ren, Z. Fang, X. Lu, E. Lewis, G. Farrell, J. Yang, P. Wang, *Sci. Rep.* **2017**, *7*, 1783.
[17] Y. Wei, Z. Gao, X. Yun, H. Yang, Y. Liu, G. Li, *Chem. Mater.* **2020**, *32*, 8747.
[18] I. V. Berezovskaya, V. P. Dotsenko, A. S. Voloshinovskii, S. S. Smola, *Chem. Phys. Lett.* **2013**, *585*, 11.
[19] J. Cao, J. Peng, L. Wang, H. Luo, X. Wang, P. Xiong, Y. Wang, M. Peng, *J. Mater. Chem. C* **2019**, *7*, 2076.
[20] Y. Gao, B. Wang, L. Liu, K. Shinozaki, *J. Lumin.* **2021**, *238*, 118235.
[21] Q. Bai, S. Zhao, L. Guan, Z. Wang, P. Li, Z. Xu, *Cryst. Growth Des.* **2018**, *18*, 3178.
[22] L. Zhang, S. Zhang, Z. Hao, X. Zhang, G.-h. Pan, Y. Luo, H. Wu, J. Zhang, *J. Mater. Chem. C* **2018**, *6*, 4967.
[23] F. Zhao, H. Cai, Z. Song, Q. Liu, *Chem. Mater.* **2021**, *33*, 3621.
[24] F. Zhao, Z. Song, J. Zhao, Q. Liu, *Inorg. Chem. Front.* **2019**, *6*, 3621.
[25] L. Yao, Q. Shao, S. Han, C. Liang, J. He, J. Jiang, *Chem. Mater.* **2020**, *32*, 2430.
[26] X. Wang, Z. Wang, M. Zheng, J. Cui, Y. Yao, L. Cao, M. Zhang, Z. Yang, H. Suo, P. Li, *Dalton Trans.* **2021**, *50*, 311.
[27] X. Zhou, J. Xiang, J. Zheng, X. Zhao, H. Suo, C. Guo, *Mater. Chem. Front.* **2021**, *5*, 4334.
[28] L. Yao, Q. Shao, M. Shi, T. Shang, Y. Dong, C. Liang, J. He, J. Jiang, *Adv. Opt. Mater.* **2021**, *10*, 2102229.
[29] P. Dorenbos, *J. Lumin.* **2005**, *111*, 89.
[30] H. Cai, S. Liu, Z. Song, Q. Liu, *J. Mater. Chem. C* **2021**, *9*, 5469.
[31] C. Liu, Z. Xia, M. Chen, M. S. Molokeev, Q. Liu, *Inorg. Chem.* **2015**, *54*, 1876.
[32] B. Malysa, A. Meijerink, T. Jüstel, *J. Lumin.* **2018**, *202*, 523.
[33] Y. Tanabe, *J. Phys. Soc. Jpn.* **1954**, *9*, 5.
[34] V. Bachmann, C. Ronda, O. Oeckler, W. Schnick, A. Meijerink, *Chem. Mater.* **2009**, *21*, 316.
[35] X. Liu, Z. Song, Y. Kong, S. Wang, S. Zhang, Z. Xia, Q. Liu, *J. Alloys Compd.* **2019**, *770*, 1069.
[36] L. You, R. Tian, T. Zhou, R.-J. Xie, *Chem. Eng. J.* **2021**, *417*, 129224.
[37] M. Back, E. Trave, J. Ueda, S. Tanabe, *Chem. Mater.* **2016**, *28*, 8347.
[38] H. Zeng, T. Zhou, L. Wang, R.-J. Xie, *Chem. Mater.* **2019**, *31*, 5245.